photonics

MDPI

Article

Slotted Nanocircuit-Enhanced Dual-Band Chiral Metasurface for Tunable Mid-Infrared Circular Dichroism

Xintao Gao [1,2,3,4], Fengji Wu [2,3,4], Shifeng Dai [2,3,4], Musheng Chen [2,3,4], Yongxi Zeng [2,3,4], Yanzhong Yu [2,3,4] and Pinghui Wu [1,2,3,4,*]

1 School of Advanced Manufacturing, Fuzhou University, Fuzhou 350108, China; gxt1311086020@163.com
2 Key Laboratory of Information Functional Material for Fujian Higher Education, Quanzhou Normal University, Quanzhou 362000, China; 15671200023@163.com (F.W.); dsf0114@163.com (S.D.); tcms@qztc.edu.cn (M.C.); zengyongxi@qztc.edu.cn (Y.Z.); yuyanzhong059368@163.com (Y.Y.)
3 Fujian Provincial Key Laboratory for Advanced Micro-Nano Photonics Technology and Devices, Quanzhou Normal University, Quanzhou 362000, China
4 Fujian Provincial University Engineering Research Center for Intelligent Optical Fiber Sensing and Testing Technology, Quanzhou Normal University, Quanzhou 362000, China
* Correspondence: phwu@zju.edu.cn; Tel.: +86-177-0505-3925

Abstract

Multi-band circular dichroism (CD) with spectral tunability is highly desirable for chiral metasurface-based sensing and polarization control. In this work, we propose a mid-infrared (MIR) metal–insulator–metal (MIM) chiral metasurface absorber composed of gold-alumina-gold (Au-Al_2O_3-Au) layers, where chirality is introduced by symmetry breaking between two gold elliptical bars in the top layer. Finite element calculations show that the structure operates over 3.5–6.5 μm and produces dual-band CD responses with values of 0.83 and −0.81. The CD magnitude in each band can be independently tuned by adjusting the semi-major or semi-minor axis of the elliptical bars. In addition, rectangular slots inserted into the bars enable continuous redshift of the resonance wavelengths, and the tunability can be further enhanced by optimizing the slot dimensions. These results provide a practical strategy for designing tunable dual-band chiral absorbers and may be useful for future chiral sensing and polarization imaging applications.

Keywords: mid-infrared; circularly-polarized waves; chiroptical metasurface; tunable dual-band

1. Introduction

Chirality is a fundamental property of natural matter and is widely observed in amino acids, DNA molecules, and odor compounds. It is characterized by mirror asymmetry, whereby a chiral structure cannot be superimposed onto its mirror image, resulting in left- and right-handed enantiomers that often exhibit distinct physical and chemical functionalities. Owing to this intrinsic structural asymmetry, chirality plays an important role in a broad range of applications, including pharmaceutical development [1–3], biological sciences [4–7], and sensing technologies [8–12]. From an optical perspective, chirality manifests as differential absorption of circularly polarized (CP) light, leading to a measurable CD response.

Nevertheless, the optical chirality exhibited by natural materials is generally weak, primarily due to their subwavelength molecular dimensions and limited dielectric contrast [13,14]. To overcome these inherent constraints, artificially engineered chiral metasurfaces have emerged as a powerful and flexible alternative. In contrast to natural chiral

Check for updates

Received: 7 April 2026
Revised: 29 April 2026
Accepted: 12 May 2026
Published: 14 May 2026

Copyright: © 2026 by the authors. Licensee MDPI, Basel, Switzerland. This article is an open access article distributed under the terms and conditions of the Creative Commons Attribution (CC BY) license.

media, chiral metasurfaces derive their key advantage from artificially designed subwavelength unit cells, such as inverse-S geometries [15], U-shaped split-ring resonators [16,17], and wavy rectangular structures [18]. Through electromagnetic resonances supported by these engineered architectures, geometric chirality can be effectively translated into strong chiroptical responses, enabling CD values that significantly exceed those achievable in natural materials. As a result, chiral metasurfaces have enabled a wide range of functional photonic devices, including chiral imaging systems [19,20], chiral light emitters [21–24], and chiral absorbers [25–29].

In recent years, substantial progress has been made in the development of MIR chiral metasurfaces. For example, in 2022, Li et al. reported an η-shaped chiral metasurface absorber based on the phase-change material vanadium dioxide (VO_2), in which active tunability of the CD response was achieved by varying the volume fraction of VO_2, covering a spectral range from 5 to 15 μm [30]. In 2024, Gao et al. proposed a near-infrared chiral absorber employing a MIM configuration, which enabled selective absorption in two distinct wavelength bands of 1500–1750 nm and 2250–2750 nm [31]. Subsequently, in 2025, Xu et al. introduced a MIR chiral metasurface composed of plasmonic double-trapezoidal prism arrays with asymmetric geometries, supporting quasi-symmetry-protected bound states in the continuum (BIC) and yielding high CD values around 4.9 μm [32]. In the same year, Xu et al. designed a chiral plasmonic metasurface based on In_3SbTe_2 (IST), consisting of asymmetric L-shaped and I-shaped resonator arrays, which enabled broadband chiroptical responses spanning the 3–7 μm range and demonstrated strong potential for infrared polarization detection and counter-detection applications [33]. Additionally, Sharma et al. reported a perovskite-based chiral optical metasurface capable of generating pronounced CD responses across three independent spectral bands. Exploiting this multi-band functionality, they further developed three types of biosensors, thereby providing a versatile platform for biomedical applications beyond the constraints of conventional single-band designs [34]. In 2026, Sun et al. presented an anisotropic thermal metasurface that enables helicity-switchable and wavelength-tunable circularly polarized coherent thermal emission in the mid-infrared region. By engineering a pair of high-Q quasi-guided-mode resonances with opposite chirality, they experimentally demonstrated high temporal coherence and strong emission circular dichroism over a wavelength range of approximately 100 nm through a temperature variation of 250 K [35].

Despite these advances, achieving independent control over CD responses in multiple bands while maintaining high CD values and spectral tunability remains a challenge. In this work, we propose a dual-band chiral metasurface absorber based on an Au–Al_2O_3–Au MIM configuration, where chiroptical activity is induced by geometric asymmetry between two coupled elliptical bars in the top layer. The designed metasurface exhibits high CD values of 0.83 and −0.81 in two distinct MIR bands, with independent control over the CD sign and magnitude achieved by adjusting the elliptical bar dimensions. Furthermore, we demonstrate continuous spectral tuning of the chiral resonances by introducing rectangular slots at the centers of the elliptical bars, enabling flexible modulation of the CD response across the 3.5–6.5 μm range.

2. Structure Design and Simulation Methods

The proposed dual-band chiral metasurface absorber is based on an Au-Al_2O_3-Au multilayer configuration. The proposed dual-band chiral metasurface is designed on a silicon substrate and consists of a 50 nm thick Au bottom mirror, a 250 nm thick Al_2O_3 spacer layer, and a 55 nm thick metasurface layer composed of dimer elliptical Au resonators.

The top view of the metasurface unit cell is shown in Figure 1b. The lattice periods along the *x*- and *y*-directions are P_x = 3.8 μm and P_y = 2 μm, respectively. The semi-

major and semi-minor axes of the slanted elliptical bar, which is rotated by an angle θ, are denoted as m_1 and m_2, respectively, while those of the vertical elliptical bar are denoted as n_1 and n_2. The presence of the slanted elliptical bar breaks the mirror symmetry of the unit cell, forming a chiral configuration that induces pronounced chiroptical responses under MIR illumination. Each elliptical bar supports two plasmonic resonances along its principal axes, thereby enabling a dual-band chiroptical response. Owing to the symmetry-breaking dimer configuration, distinct electric-field resonance modes are excited under left-circularly polarized (LCP) and right-circularly polarized (RCP) MIR illumination, resulting in polarization-dependent absorption intensities. Furthermore, the top and bottom Au layers together form a Fabry-Pérot cavity, which confines the incident light through multiple reflections and excites resonant modes that significantly enhance both circular dichroism and optical absorption.

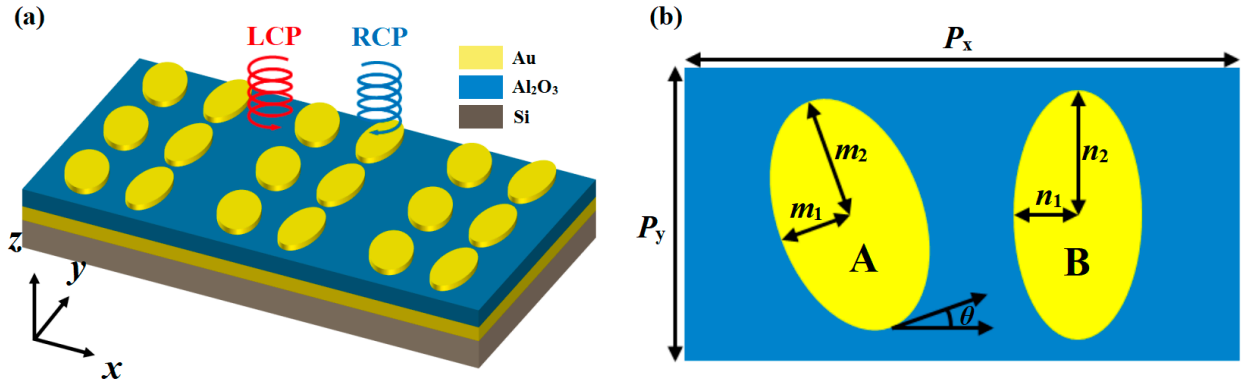

Figure 1. (**a**) Schematic diagram of the proposed dual-band chiral metasurface absorber. (**b**) Top view of unit cell with two coupled elliptical bars.

A possible fabrication route for the proposed dual-band chiral metasurface absorber is illustrated in Figure 2. The process starts with standard cleaning of a silicon substrate, followed by the deposition of a 50 nm thick Au bottom mirror and a 250 nm thick Al_2O_3 spacer layer. Then, a sufficiently thick positive photoresist or electron-beam resist is spin-coated onto the spacer layer to serve as a temporary pattern-transfer mask. After lithographic exposure and development, the resist defines an opening pattern corresponding to the designed metasurface geometry. Subsequently, a 55 nm thick Au layer is deposited, preferably by a directional evaporation process, and a lift-off step is performed to remove the resist together with the unwanted Au on top of it, leaving the designed dimer elliptical resonators on the Al_2O_3 spacer.

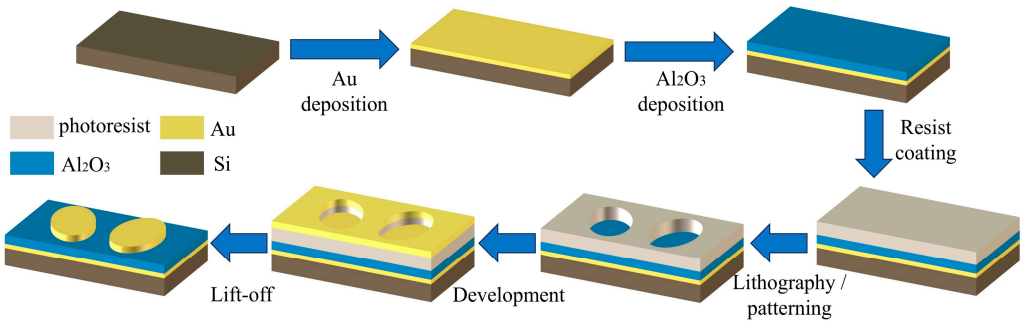

Figure 2. Schematic illustration of the possible fabrication route for the proposed dual-band chiral metasurface absorber.

To investigate the influence of different resonance modes, four Au-Al_2O_3-Au dual-band chiral metasurface absorbers with distinct geometric parameters were designed by

varying the relative lengths of the semi-major and semi-minor axes of the two elliptical bars. Each structure exhibits unique absorption characteristics under LCP and RCP illumination, leading to different CD responses. The corresponding geometric parameters are summarized in Table 1.

Table 1. Basic parameters of the dual-band chiral metasurface.

Structure	Θ (°)	m_1 (μm)	m_2 (μm)	n_1 (μm)	n_2 (μm)
1	20	0.5	0.82	0.445	0.78
2	20	0.5	0.82	0.505	0.78
3	20	0.5	0.82	0.505	0.85
4	20	0.5	0.82	0.44	0.85

Numerical calculations of the metasurface absorbers near their resonance peaks were performed using the finite element method (FEM). A circularly polarized plane wave was normally incident along the *z*-direction. Perfectly matched layers (PMLs) were placed at the upper and lower boundaries of the metasurface along the *z*-direction to absorb outgoing waves and suppress artificial reflections from the open boundaries. Additionally, periodic boundary conditions (PBCs) were applied to the four lateral boundaries of the unit cell along the *x*- and *y*-directions to model an infinitely periodic metasurface array. To ensure the accuracy and reliability of the numerical results, the FEM calculations were carried out with a minimum mesh size of 40 nm. The permittivity of Al_2O_3 was taken from experimentally measured data [36], whereas the optical constants of Au were adopted from the experimental data reported by Babar and Weaver [37]. According to the optical constants of Au reported by Babar and Weaver, the corresponding skin depth in the 3.5–6.5 μm range is only about 10–12 nm. Therefore, the 50 nm Au layer is still several skin depths thick and can effectively suppress transmission. Accordingly, the Au bottom mirror can be treated as optically opaque, and the normalized absorption A of the absorber can be calculated as $A = 1 - R$, where R denotes the normalized reflection.

3. Results and Discussions

Figure 3a–d presents the calculated absorption spectra of the four metasurface structures with different elliptical bar geometries under LCP and RCP illumination. Four distinct absorption behaviors are observed within the dual wavelength ranges of 4–4.75 μm and 4.75–6 μm. Specifically, Figure 3a presents the absorption spectrum of Structure 1, with n_1 = 0.445 μm and n_2 = 0.78 μm. The spectrum exhibits two chiral resonance peaks in the 4–4.75 μm and 4.75–6 μm bands, respectively. In this case, the absorption intensity under RCP illumination is significantly higher than that under LCP illumination in both bands. When n_1 is increased to 0.505 μm while n_2 is maintained at 0.78 μm (Structure 2), opposite chiral absorption characteristics are observed in the two wavelength bands. As shown in Figure 3b, within the 4.75–6 μm band, the absorption intensity of RCP light remains higher than that of LCP light, whereas the opposite behavior occurs in the 4–4.75 μm band. Subsequently, when n_1 is fixed at 0.505 μm and n_2 is further increased to 0.85 μm (Structure 3), the absorption spectrum shown in Figure 3c displays stronger absorption for LCP light than for RCP light in both wavelength bands. Finally, in Structure 4, where n_1 is readjusted to 0.44 μm while n_2 is largely maintained at 0.85 μm, the two wavelength bands again exhibit opposite chiral absorption responses. As illustrated in Figure 3d, RCP light exhibits higher absorption than LCP light in the 4–4.75 μm band, whereas the reverse trend occurs in the 4.75–6 μm band. These results demonstrate that, by tailoring the geometric parameters of the coupled elliptical bars, a dual-band chiral absorber with two independently controllable absorption peaks can be realized.

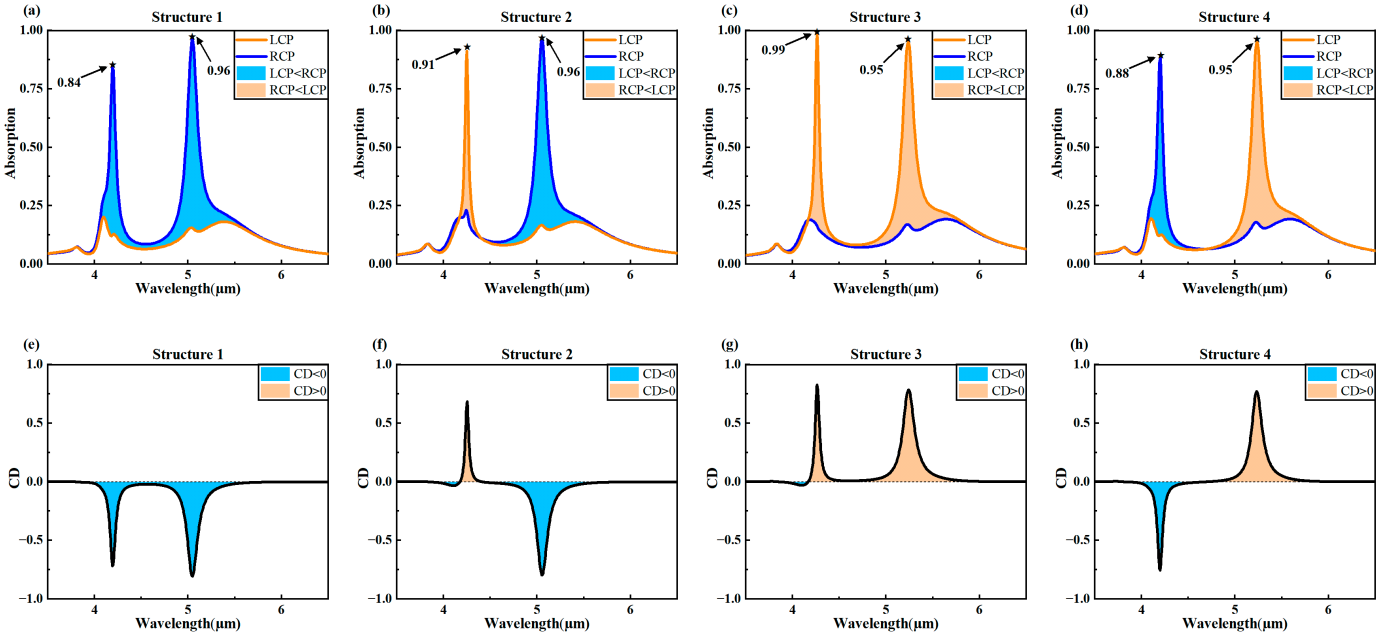

Figure 3. (**a**–**d**) Chiroptical absorption spectra and (**e**–**h**) CD spectra for the Au-Al_2O_3-Au chiroptical metasurface absorber with geometric parameters listed in Table 1 (The star symbols indicate the peak positions of the spectra).

To quantitatively characterize the chiral response of the proposed metasurface, the CD is calculated, which is defined as the difference between the absorption under LCP and RCP illumination. The CD is calculated using the following expression:

$$\mathrm{CD} = A_{\mathrm{LCP}} - A_{\mathrm{RCP}}, \tag{1}$$

where A_{LCP} and A_{RCP} denote the normalized absorption under LCP and RCP illumination, respectively. When the absorption under LCP illumination exceeds that under RCP illumination, the CD value is positive; otherwise, it is negative.

Figure 3e–h presents the CD spectra of the metasurface for the four structural configurations. By independently adjusting the semi-minor axis n_1 and semi-major axis n_2 of elliptical bar B, the CD magnitude and sign can be selectively controlled within the wavelength bands of 4–4.75 μm and 4.75–6 μm. In Structure 1, where $n_1 < m_1$ and $n_2 < m_2$, the CD values remain negative in both wavelength bands. Compared with Structure 1, Structure 2 features an increased semi-minor axis n_1 such that $n_1 > m_1$, while n_2 remains unchanged. This modification causes the CD in the 4–4.75 μm band to become predominantly positive, while the CD in the 4.75–6 μm band remains negative. This behavior indicates that the n_1 predominantly influences the CD response in the shorter-wavelength band. Structure 3 is obtained by further increasing n_2, resulting in predominantly positive CD values in both wavelength bands. This observation demonstrates that n_2 primarily governs the CD response in the longer-wavelength band. These conclusions are further corroborated by Structure 4, in which $n_1 < m_1$ and $n_2 > m_2$ lead to negative CD values in the 4–4.75 μm band and positive CD values in the 4.75–6 μm band.

From the above analysis, it can be concluded that variations in the semi-minor axis n_1 and semi-major axis n_2 of elliptical bar B directly modulate the absorption characteristics for both LCP and RCP light. In the following analysis, the relationship between CD values and geometric parameters is examined.

Structure 4, which exhibits two strong CD peaks with opposite signs, is selected as a representative example for further analysis. Figure 4a shows the CD spectra of the metasurface in the 3.5–6.5 μm range for different rotation angles θ of elliptical bar A from

0° to 90°. Two key observations can be made. First, the resonance wavelengths remain nearly unchanged throughout the rotation process, indicating that θ mainly modulates the chiroptical strength rather than the resonance positions. Second, the CD response is strongly dependent on the rotation angle and exhibits distinct evolution trends in the two spectral bands. For the short-wavelength band, the CD value starts from nearly zero at $\theta = 0°$, decreases to a negative minimum at $\theta = 20°$, then gradually approaches zero and reverses sign at $\theta = 40°$. As θ further increases, the short-wavelength CD becomes positive, reaches a maximum at $\theta = 60°$, and then decreases continuously, becoming nearly zero again at $\theta = 90°$. For the long-wavelength band, the CD response remains positive over the whole angular range: it increases from nearly zero at $\theta = 0°$ to a maximum at $\theta = 20°$, then decreases gradually and becomes almost zero at $\theta = 70°$, remaining negligible from 70° to 90°. These results confirm that θ is a key parameter for controlling both the sign and magnitude of the dual-band CD response. In particular, the two limiting cases of $\theta = 0°$ and $\theta = 90°$ correspond to a strongly weakened chiral asymmetry in the unit cell. At $\theta = 0°$, the in-plane asymmetry is nearly removed, so the symmetry-breaking interaction responsible for the chiroptical response becomes negligible and the CD peaks approach zero. A similar situation occurs at $\theta = 90°$, where the resonator orientation again approaches a nearly symmetric configuration in the projected unit cell, leading to a substantial cancelation of the chiral coupling and a vanishing CD response. Therefore, the observed CD evolution with θ is governed by the progressive breaking and recovery of the in-plane asymmetry between the two elliptical resonators, and the maximum chiroptical contrast appears only within an intermediate angular range.

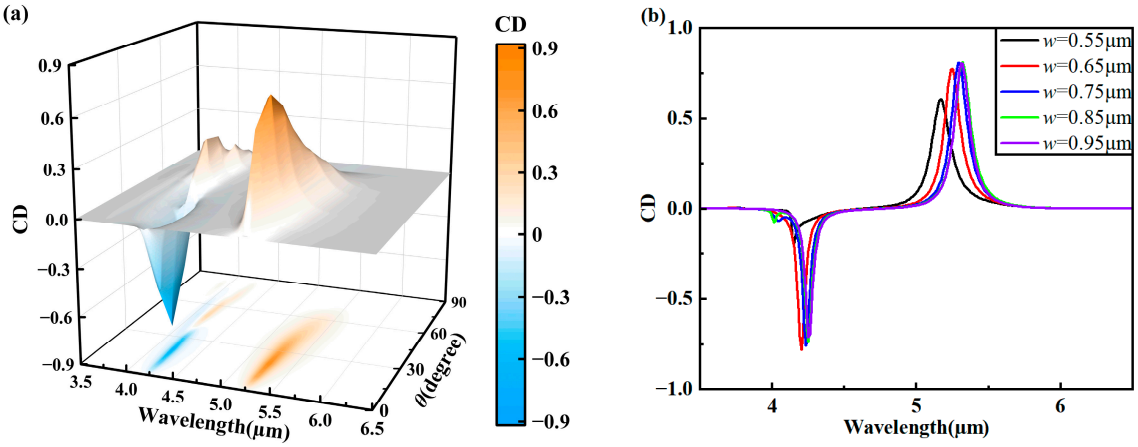

Figure 4. CD spectral mapping for Structure 4 as a function of (**a**) rotation angle θ and (**b**) inter-ellipse separation w.

In addition to the rotation angle θ, the inter-ellipse separation w also influences the CD response, as shown in Figure 4b. When $w = 0.55$ μm, CD resonance is significantly suppressed, with the short-wavelength peak reduced to approximately one quarter of the corresponding values in the other cases and the long-wavelength peak reduced to about two-thirds. This indicates that an overly small separation weakens the optimal chiral coupling between the two elliptical resonators. As w increases to 0.65 μm, the short-wavelength CD peak reaches the largest absolute value, while the long-wavelength peak remains comparable to that in the other cases. For $w = 0.75$ μm, 0.85 μm, and 0.95 μm, the CD spectra are nearly overlapped, suggesting that the inter-resonator coupling has become relatively insensitive to further increases in w within this range. This result confirms that the inter-ellipse distance mainly acts as a coupling-tuning parameter.

Figure 5 further illustrates the dependence of the CD response on n_1 and n_2. As shown in Figure 5a, with n_2 fixed at 0.85 μm and n_1 increasing from 0.4 μm to 0.55 μm, the CD peak near 5.2 μm remains consistently positive, while the CD peak near 4.2 μm gradually shifts from negative to positive. In contrast, Figure 5b shows that when n_1 is fixed at 0.44 μm and n_2 increases from 0.75 μm to 0.9 μm, the CD peak near 4.2 μm remains negative, whereas the peak near 5.2 μm transitions from negative to positive, accompanied by a slight redshift in the resonance wavelength. Except near the transition regions, the absolute value of the CD remains above 0.75. These results confirm that the dual-band chiral response is preserved under geometric variations and that the sign of each CD peak can be independently controlled through precise adjustment of n_1 or n_2.

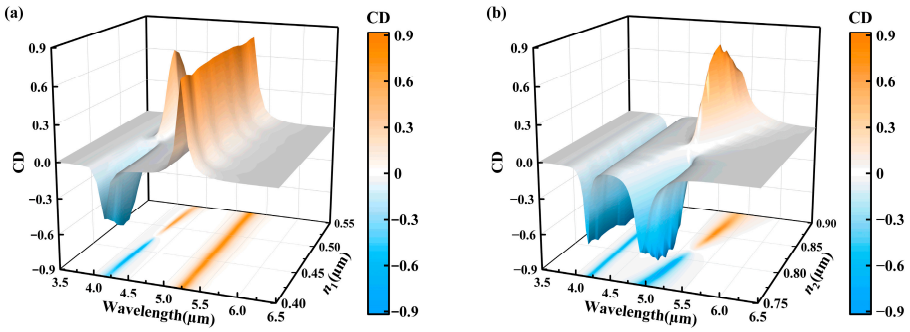

Figure 5. CD spectral mapping for Structure 4 as a function of (**a**) semi-minor axis n_1 and (**b**) semi-major axis n_2.

To gain insight into the physical mechanism underlying the observed chiroptical responses, the influence of the lattice periods and the incident angle on the CD response was investigated. As shown in Figure 6a, varying P_x mainly shifts the shorter-wavelength negative CD resonance, while the longer-wavelength positive resonance is only slightly modified. In contrast, Figure 6b shows that P_y has a stronger influence on the longer-wavelength resonance, whereas the shorter-wavelength band remains comparatively stable. This anisotropic dependence indicates that the two chiral resonances are associated with different in-plane current pathways and coupling strengths along the orthogonal lattice directions. Moreover, as shown in Figure 6c, the CD response reaches its maximum at normal incidence and gradually weakens as the incident angle α increases in the x–z plane. The oblique incidence reduces the overlap between the incident circularly polarized field and the asymmetric resonator currents, thereby weakening the symmetry-breaking excitation and the associated cavity-assisted resonance. These results suggest that the proposed metasurface operates through a hybrid localized plasmonic and Fabry–Pérot cavity mechanism optimized for normal incidence.

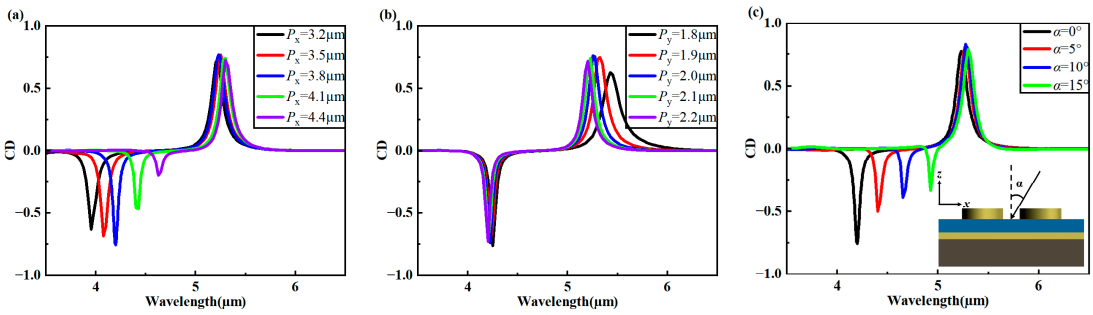

Figure 6. CD spectral mapping for Structure 4 as a function of (**a**) the lattice period along the x-direction, (**b**) the lattice period along the y-direction and (**c**) incident angles α.

To further clarify the resonance mechanism, we calculated the electric field distributions on the upper surface of the Al_2O_3 spacer layer at the resonance wavelengths for each structure, as shown in Figure 7. Owing to the coupled elliptical-bar configuration, four distinct resonant modes are excited at two separate wavelengths under CP illumination, with electric fields primarily concentrated along the edges of the elliptical bars. As shown in Figure 7a, in Structure 1, both the semi-major and semi-minor axes of elliptical bar B are shorter than those of bar A. This geometric asymmetry leads to distinct resonance behaviors under CP illumination. At both resonance wavelengths, the electric-field intensity under RCP illumination is stronger than that under LCP illumination, indicating a stronger resonance for RCP light. The electric-field distributions of Structure 2 are shown in Figure 7b. In this case, the semi-major axis n_2 of bar B remains unchanged, while the semi-minor axis n_1 increases to 0.505 μm, exceeding m_1. Consequently, different resonance modes are excited under LCP and RCP illumination. At 5.01 μm, the electric-field distribution resembles that of Structure 1, whereas at 4.24 μm, the electric-field intensity under LCP illumination becomes stronger than that under RCP illumination, opposite to the behavior observed in Structure 1. In Structure 3, the situation is reversed relative to Structure 1, as both n_1 and n_2 of bar B are larger than m_1 and m_2 of bar A. As shown in Figure 7c, resonance peaks occur at 4.25 μm and 5.20 μm, with significantly stronger electric-field intensity under LCP illumination across both wavelengths. Finally, in Structure 4, the electric-field distribution is opposite to that of Structure 2, with $n_1 < m_1$ and $n_2 > m_2$. As shown in Figure 7d, at 4.19 μm, the electric-field intensity under LCP illumination is weaker than that under RCP illumination, whereas at 5.20 μm, the opposite behavior is observed. Among the two coupled elliptical bars, the tilted bar A plays a critical role in breaking the structural symmetry of the metasurface, thereby inducing a strong chiral response under CP illumination. By adjusting the semi-major and semi-minor axes of bar B, selective switching of chiral absorption can be achieved across the two wavelength bands.

In more detail, each elliptical bar supports anisotropic plasmonic dipole modes along its principal axes. Under circularly polarized illumination, these modes are excited with different amplitudes and phases, leading to asymmetric surface-current distributions on the top Au layer. Meanwhile, the Au back reflector and the Al_2O_3 spacer form a Fabry–Pérot-like cavity, which confines the electromagnetic field near the metal–dielectric interfaces and enhances the chiroptical contrast. Therefore, the observed CD response originates from the interplay between symmetry-breaking resonator coupling, localized plasmonic excitation, and cavity feedback, rather than from a single isolated resonance channel.

Based on the above physical interpretation, it is also necessary to assess whether the proposed chiroptical response can remain stable under reasonable fabrication-related deviations and numerical discretization. Therefore, we further analyzed the thickness tolerance of the top Au metasurface layer and the mesh convergence of the FEM calculations.

Figure 8a shows the calculated CD spectra obtained by varying the thickness of the top Au metasurface layer from 35 nm to 75 nm around its nominal value of 55 nm, while keeping all other parameters unchanged. The spectra exhibit only negligible variations in both resonance wavelengths and CD magnitudes, indicating that the proposed design maintains stable chiroptical performance over a relatively wide thickness range. This result suggests that the metasurface has a robust fabrication tolerance with respect to moderate deposition fluctuations in the top Au metasurface layer.

As shown in Figure 8b, three mesh levels with element sizes of 270 nm, 100 nm, and 6 nm were used to evaluate the numerical convergence. The coarse mesh (270 nm) leads to a slight decrease in the CD peak values and a minor shift in the resonance wavelengths, whereas the medium mesh (100 nm) and fine mesh (6 nm) produce nearly identical spectra.

This indicates that the results are sufficiently converged when the mesh size is reduced to 100 nm. and that the selected mesh is sufficient for the calculations.

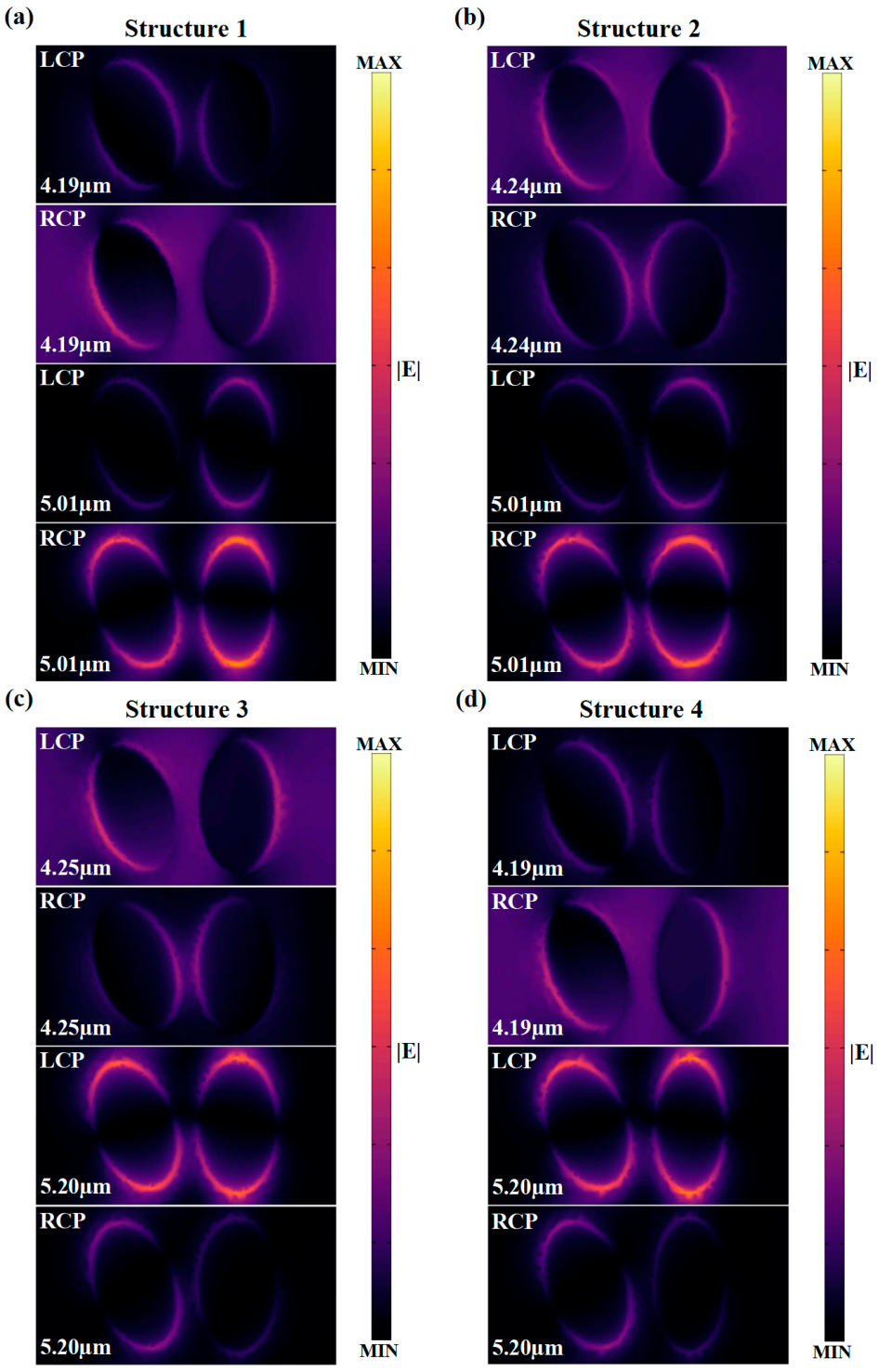

Figure 7. Calculated electric field distribution at the interface between the top Au layer and dielectric spacer layer for Structures 1–4 at two chiral resonance wavelengths within the 4–4.75 μm and 4.75–6 μm bands (**a**–**d**).

Furthermore, continuous tuning of the chiral resonance wavelength can be achieved by introducing slotted nanocircuit structures into the resonators. Here, the term "nanocircuit" refers to an equivalent electromagnetic circuit implemented at the nanoscale, rather than an actual electrical circuit. This strategy is based on the electric-field continuity

condition at high-index-contrast interfaces, which has been widely employed to enhance electromagnetic field confinement in high-refractive-index materials [38–40].

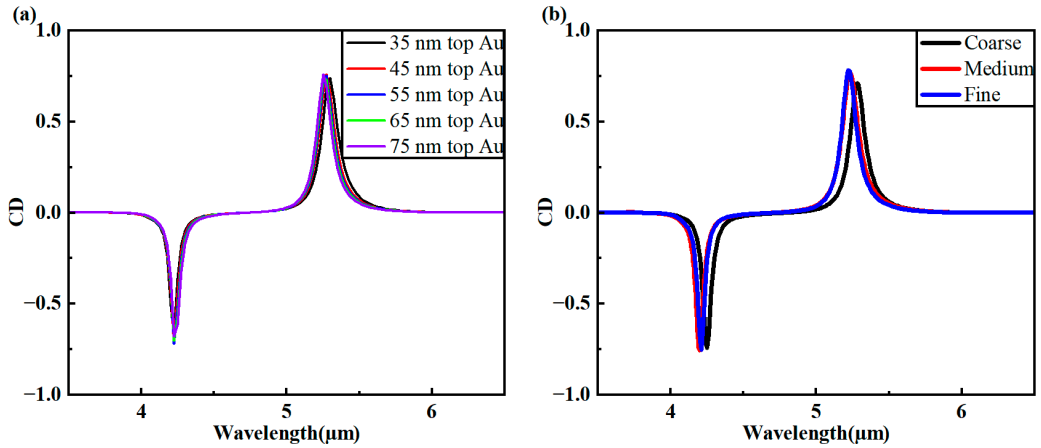

Figure 8. CD spectral mapping for Structure 4 as a function of (**a**) different thickness values of the top Au metasurface layer and (**b**) different mesh levels.

In this work, rectangular slots are introduced at the centers of both elliptical bars A and B, as illustrated in Figure 9a. The corresponding top view of the unit cell is shown in Figure 9b, where the slot length and width are denoted by L and W, respectively, and the slot depth equals the thickness of the top Au layer. In this structure, the Au elliptical bars act as an inductive current path, while the rectangular slots introduce a capacitive discontinuity that redistributes the surface current and local electric field, thereby modifying the effective LC response and shifting the resonance wavelength.

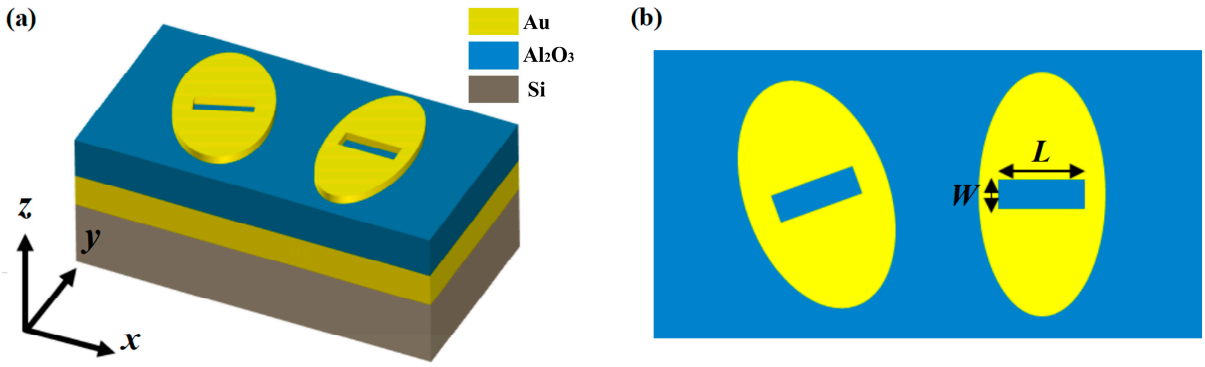

Figure 9. (**a**) Schematic diagram of the CD slotted metasurface structure. (**b**) Top view of the slotted elliptical metasurface unit cell with slot parameters L and W.

A possible fabrication route for the slotted chiral metasurface is shown in Figure 10. Compared with the unslotted structure, the only difference is that the rectangular slot is included in the same top-layer lithography pattern as the elliptical resonator. Therefore, the slot and ellipse are co-defined in a single patterning step, which significantly reduces the relative-position error between them. The subsequent Au deposition and lift-off process then yield the final slotted metasurface.

Using Structure 4 as an example, Figure 11 presents the corresponding CD responses under LCP and RCP illumination for different values of the slot length L. With the slot width fixed at W = 0.1 μm, the slot length L is gradually increased to 0.75 μm, the resonance peak near 4.2 μm remains nearly unchanged, whereas the resonance near 5.2 μm exhibits a pronounced redshift that becomes more significant with increasing L. This selective

sensitivity indicates that the long-wavelength mode is associated with a current distribution that overlaps more strongly with the slot along the major-axis direction of the resonator.

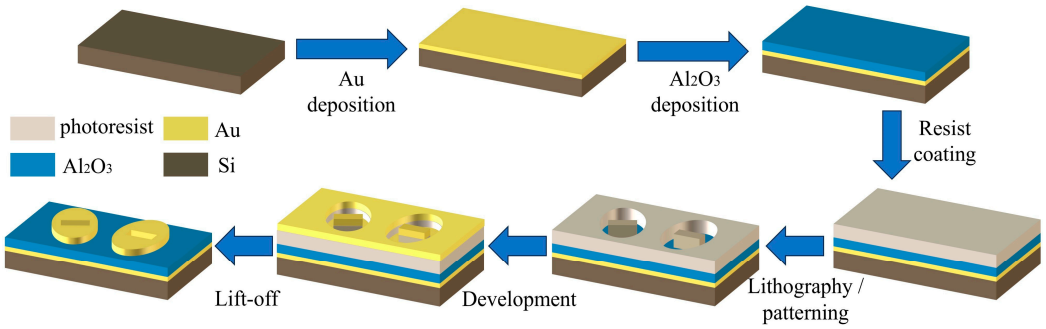

Figure 10. Schematic illustration of a possible fabrication route for the slotted dual-band chiral metasurface absorber.

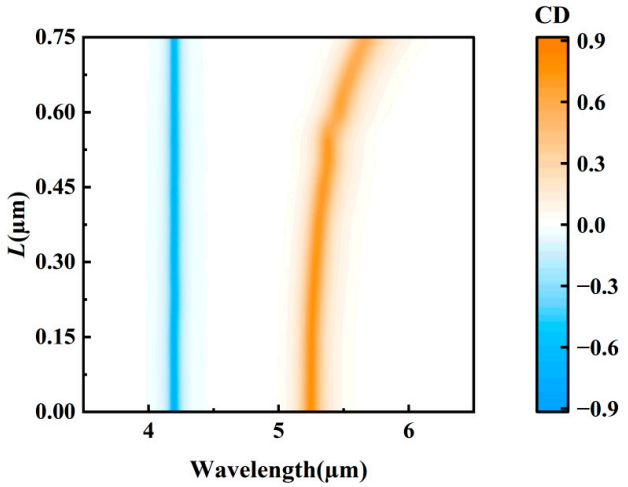

Figure 11. CD spectra for Structure 4 with varying slot length L (W = 0.1 μm).

Figure 12 shows the corresponding results for variations in the slot width W, with L fixed at 0.6 μm. In this case, the resonance near 4.2 μm exhibits a redshift with increasing W, while the magnitude of the redshift at 5.2 μm gradually diminishes as W increases. The longer-wavelength resonance near 5.2 μm exhibits a more pronounced redshift, indicating stronger sensitivity to the transverse capacitive interruption introduced by W. The shorter-wavelength resonance also redshifts as W increases. Therefore, W does not selectively tune only the long-wave band; rather, it modulates both bands simultaneously, with a stronger effect on the long-wavelength mode and a weaker effect on the short-wavelength mode. This behavior confirms that the two chiral resonances originate from distinct hybrid current channels with different spatial field localizations and symmetry properties. This provides an additional degree of freedom for tailoring the chiroptical response of the metasurface.

Finally, as summarized in Table 2, the performance of the proposed chiral metasurface is compared with previously reported designs. The results indicate that the present metasurface exhibits superior CD performance within the target wavelength range compared with other metasurfaces operating in the same spectral region, maintaining a balanced performance with both the maximum and minimum CD values exceeding 0.8 in absolute value. Additionally, the present metasurface exhibits stronger spectral selectivity. Within the target band, the CD response is close to zero away from the resonance peaks, indicating cleaner dual-band discrimination. Overall, the proposed metasurface achieves a strong dual-band CD response across the 3.5–6.5 μm MIR range. The introduction of rectangular

slots further enhances spectral tunability, highlighting the potential of this design for MIR chiral sensing applications.

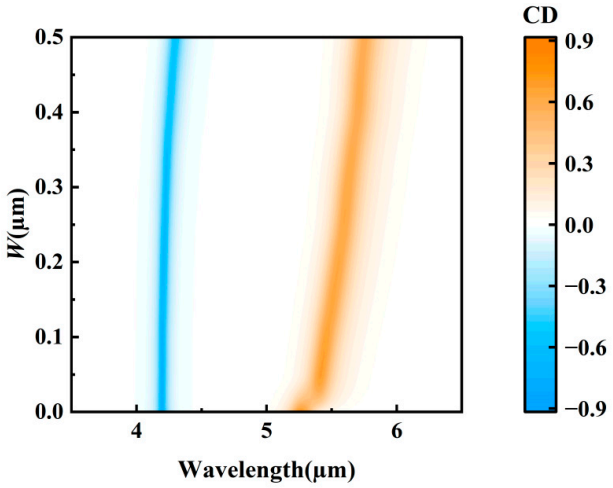

Figure 12. CD spectra for Structure 4 with varying slot width W (L = 0.6 μm).

Table 2. Comparison of the proposed chiral metasurface with previously reported chiral metamaterial absorbers. All listed CD values are absorption-based CD, as defined in Equation (1).

Reference	Structure	CD Type	Spectra Range (μm)	Maximum CD	Minimum CD
[25]	MIM	Single-band	5–5.5	0.6	0.56
[39]	MIM	Dual-band	3–5	0.8	−0.74
[41]	MIM	Single-band	5–5.9	0.63	0.57
[42]	MIM	Dual-band	4–6	0.6	−0.55
This work	MIM	Dual-band	3.5–6.5	0.83	−0.81

The proposed metasurface may be useful for mid-infrared circular-polarization detection and chiral sensing. The strong dual-band selectivity and near-zero off-resonance CD response also suggest potential use in narrowband polarization filtering and compact chiroptical photonic integration.

4. Conclusions

In conclusion, we have proposed and numerically demonstrated a mid-infrared dual-band chiral metasurface absorber exhibiting high circular dichroism. By incorporating two asymmetric Au elliptical bars in the top layer of an MIM configuration, the metasurface achieves dual-band chiral selectivity and tunability under both LCP and RCP illumination. Independent control over the sign of the CD response in the two wavelength bands is realized by adjusting the semi-major and semi-minor axes of the vertical elliptical bars, with the maximum CD magnitude reaching 0.83. CD spectral mapping further confirms the strong dependence of the chiroptical response on the geometric parameters of the metasurface. Moreover, the introduction of rectangular slots at the centers of the elliptical bars enhances the tunability of the MIR CD response across the 3.5–6.5 μm range by enabling continuous spectral redshifts of the resonance bands. These results demonstrate that the slotted elliptical-bar configuration allows flexible modulation of the chiroptical response through subtle geometric variations. The combination of high CD values and dual-band tunability makes the proposed metasurface a promising candidate for applications in thermal energy harvesting, optical communications, circular polarization detection, biosensing, and medical imaging.

Author Contributions: Conceptualization, X.G.; methodology, X.G.; validation, X.G., F.W. and S.D.; formal analysis, X.G.; investigation, X.G. and F.W.; resources, X.G. and S.D.; data curation, X.G.; writing—original draft preparation, X.G.; writing—review and editing, X.G., M.C., Y.Z. and P.W.; visualization, X.G.; supervision, Y.Z., Y.Y. and P.W.; project administration, M.C. and P.W.; funding acquisition, Y.Y. and P.W. All authors have read and agreed to the published version of the manuscript.

Funding: This research received no external funding.

Data Availability Statement: The original contributions presented in this study are included in the article. Further inquiries can be directed to the corresponding author.

Conflicts of Interest: The authors declare no conflicts of interest.

References

1. Jeschke, P. The continuing significance of chiral agrochemicals. *Pest Manag. Sci.* **2025**, *81*, 1697–1716. [CrossRef] [PubMed]
2. Liu, Y.; Li, X.; Zhu, Q.; Zhong, Y.; Lin, X.; Zhou, C.; Qi, C.; Guo, J.; Ma, Q.; Wu, H.; et al. Brain-Targeted Near-Infrared Chiral TeSe Nanodrug Against Orthotopic Drug-Resistant Glioma. *Angew. Chem. Int. Ed.* **2026**, *138*, e202516990. [CrossRef]
3. Xiong, Q.; Tian, K.; Liu, X.; He, L.; Song, Y.; Liu, Y.; Wang, Z.; Dong, X.; Wang, C. Stereodivergent Construction of Spiropyrrolidine-γ-Butyrolactones Enabled by Cu/Ru Sequential Catalysis and Stereoselective Reduction. *Angew. Chem. Int. Ed.* **2026**, *138*, e19537. [CrossRef]
4. Das, T.K.; Preeyanka, N.; Mishra, S.; Sang, Y.; Fontanesi, C. Spin-Selective Anisotropic Magnetoresistance Driven by Chirality in DNA. *Adv. Funct. Mater.* **2025**, *35*, 2425377. [CrossRef]
5. Wang, X.; Zhang, X.; Zhao, Y.; Wu, X.; Yang, G.; Zhao, Y.; Liu, G. Biomimetic Chiral Recognition of Biothiols by Enantiomeric Nanoclusters in Plasma. *Adv. Mater.* **2025**, *38*, e14158. [CrossRef]
6. Rosas, S.; Biswas, S.K.; Adi, W.; Kuruoglu, F.; Beisenova, A.; Patankar, M.S.; Yesilkoy, F. Mass-Manufactured Gradient Plasmonic Metasurfaces for Enhanced Mid-IR Spectrochemical Analysis of Complex Biofluids. *Adv. Mater.* **2025**, *37*, e04355. [CrossRef] [PubMed]
7. Yan, B.; Duan, M.; Chen, B.; Zheng, H.; Zhou, Y.; Zhou, G.; Zhang, S.; Wang, J.; Yao, G.; Zhu, Y.; et al. Engineering Highly Luminescent and Chiral Metal Nanoclusters with Single-Stranded DNA. *ACS Appl. Mater. Interfaces* **2025**, *17*, 42443–42453. [CrossRef]
8. Verma, O.; Adhikari, S.; Chakraborty, A.; Jain, P.K.; Link, S. Bovine-Hemoglobin Detection by Single-Particle Plasmon-Coupled Circular Dichroism. *Nano Lett.* **2025**, *25*, 8480–8487. [CrossRef]
9. Lu, Y.; Zhao, X.; Yan, D.; Mi, Y.; Sun, P.; Yan, X.; Liu, X.; Lu, G. Upconversion-based chiral nanoprobe for highly selective dual-mode sensing and bioimaging of hydrogen sulfide in vitro and in vivo. *Light Sci. Appl.* **2024**, *13*, 180. [CrossRef] [PubMed]
10. Liu, H.; Guo, R.; Li, L.; Wen, Y.; Wang, L.; Yan, J.; Liu, G. A NIR Biosensor for the Detection of Silver Ions Based on a Single-Chirality Carbon Nanotube with DNA Wrapping. *ACS Appl. Nano Mater.* **2025**, *8*, 13719–13728. [CrossRef]
11. Karim, M.E.; Zubair, A. Star-shaped nanostructure-based multifunctional chiral metasurface for near-infrared wavelengths. *Opt. Laser Eng.* **2025**, *194*, 109149. [CrossRef]
12. Lu, M.; Guo, Z.; Deng, C.; Hu, X.; Chen, M. Tunable multiband asymmetric transmission based on flexible chiral metamaterial for refractive index sensing. *J. Opt. Soc. Am. B* **2025**, *42*, 419–424. [CrossRef]
13. Yoo, S.; Park, Q.-H. Metamaterials and chiral sensing: A review of fundamentals and applications. *Nanophotonics* **2019**, *8*, 249–261. [CrossRef]
14. Lininger, A.; Palermo, G.; Guglielmelli, A.; Nicoletta, G.; Goel, M.; Hinczewski, M.; Strangi, G. Chirality in light-matter interaction. *Adv. Mater.* **2023**, *35*, e2107325. [CrossRef] [PubMed]
15. Liang, F.; Liu, X.; Zhao, Z.; Han, H.; Xi, S.; Hu, J. Design of Chiral Metasurface Sensor with Stabilized Strong Circular Dichroism. *Acta Opt. Sin.* **2025**, *45*, 0828002.
16. Yang, H.; Sun, H.; Yang, Y.; He, Q.; Xiao, G.; Wang, B.; Shao, L. Strong circular dichroism absorbers using chiral metamaterials with circular polarization. *Opt. Commun.* **2024**, *559*, 130403. [CrossRef]
17. Li, J.; Wang, D.; Xiong, R. Reconfigurable metasurface for circular dichroism and a polarization converter. *Opt. Mater. Express* **2024**, *14*, 2612–2622. [CrossRef]
18. Zeng, X.; Rosenmann, D.; Czaplewski, D.A.; Gao, J.; Yang, X. Chiral metasurfaces of wavy rectangle resonators with tunable circular dichroism. *Optik* **2023**, *286*, 171024. [CrossRef]
19. Zhu, T.; Wang, L.; Jing, W.; Deng, J.; Ye, J.; Zhang, Y.; Chu, Z.; Zhou, J.; Chen, X.; Li, X.; et al. Circular Polarimetric Imaging with a Metamaterial Integrated Long-Wavelength Infrared Focal Plane Array. *Adv. Sci.* **2025**, *12*, e09292. [CrossRef]
20. Chen, T.; Raza, F.; Ni, C.; Zhang, G.; Chen, R.; Li, X.; Dang, Y.; Zhang, S.; Ng, C.-K.; Hu, J.; et al. Thermal Digital Imaging by Chirally Coded Metasurfaces. *Laser Photonics Rev.* **2025**, *19*, 2500129. [CrossRef]

21. Wang, X.; Sentz, T.; Bharadwaj, S.; Ray, S.K.; Wang, Y.; Jiao, D.; Qi, L.; Jacob, Z. Observation of nonvanishing optical helicity in thermal radiation from symmetry-broken metasurfaces. *Sci. Adv.* **2023**, *9*, eade4203. [CrossRef]
22. Nguyen, A.; Hugonin, J.-P.; Coutrot, A.-L.; Garcia-Caurel, E.; Vest, B.; Greffet, J.-J. Large circular dichroism in the emission from an incandescent metasurface. *Optica* **2023**, *10*, 232–238. [CrossRef]
23. Nolen, J.R.; Overvig, A.C.; Cotrufo, M.; Alù, A. Local control of polarization and geometric phase in thermal metasurfaces. *Nat. Nanotechnol.* **2024**, *19*, 1627–1634. [CrossRef] [PubMed]
24. Sun, K.; Yang, B.; Cai, Y.; Kivshar, Y.; Han, Z. Circularly polarized thermal emission driven by chiral flatbands in monoclinic metasurfaces. *Sci. Adv.* **2025**, *11*, eadw0986. [CrossRef] [PubMed]
25. Mahmud, M.S.; Rosenmann, D.; Czaplewski, D.A.; Gao, J.; Yang, X. Chiral plasmonic metasurface absorbers in the mid-infrared wavelength range. *Opt. Lett.* **2020**, *45*, 5372–5375. [CrossRef]
26. Shen, Z.; Huang, D.; Lin, X. Dual-band chirality-selective absorbing by plasmonic metasurfaces with breaking mirror and rotational symmetry. *Opt. Express* **2023**, *31*, 35730–35741. [CrossRef]
27. Lv, S.; Hu, F.; Luo, W.; Xu, H.; An, L. Design of tunable selective light-absorbing metasurfaces driven by intrinsically chiral quasi-bound states in the continuum. *Opt. Express* **2024**, *32*, 30053–30064. [CrossRef] [PubMed]
28. Tan, Y.; Hu, C.; Li, M.; Yang, R. Tunable terahertz chiral absorber with graphene-metal hybrid metasurfaces. *Opt. Mater. Express* **2025**, *15*, 3025–3035. [CrossRef]
29. Kim, S.; Jang, H.; Han, J.; Lee, J.; Jun, Y.C. Ultranarrowband Chiral Absorbers in the Visible Region Based on Brillouin Zone Folding Metasurfaces. *Nano Lett.* **2025**, *25*, 2841–2849. [CrossRef]
30. Li, S.; Sang, T.; Yang, C.; Pei, Y.; Mi, Q.; Wang, Y.; Cao, G.; Liu, C. Chiral metasurface absorbers with tunable circular dichroism in the mid-infrared via phase transition of vanadium dioxide. *Opt. Commun.* **2022**, *521*, 128557. [CrossRef]
31. Gao, Z.; Wang, P.; Xu, Z.; Zhao, T. Chiral metasurface absorber with near-infrared excitation-induced dual circular dichroism. *Opt. Laser Technol.* **2024**, *175*, 110826. [CrossRef]
32. Xu, H.; Meng, Z.; Liu, Y.; Su, J.; Fang, Z.; Zhou, J. Mid-infrared bifunctional high-Q plasmonic metasurfaces with strong intrinsic chirality and imaging-based biosensing. *J. Mater. Chem. C* **2025**, *13*, 11644–11650. [CrossRef]
33. Xu, G.; Zhang, X.; Wang, W.; Zarei, M.R.; Guo, K.; Kang, Q.; Guo, Z. Dynamic manipulation of mid-infrared polarized thermal emission enabled by In_3SbTe_2 metasurfaces. *Adv. Photon. Nexus* **2025**, *4*, 68–76. [CrossRef]
34. Sharma, V.; Kalra, Y.; Sinha, R.K. Triple-band perovskite based chiral metasurface biosensor with multi-functionalities. *J. Comput. Electron.* **2025**, *24*, 97. [CrossRef]
35. Sun, K.; Qin, H.; Liu, M.; Chen, F.; Cai, Y.; Wu, P.; Qiu, C.; Han, Z. Helicity-selective and spectrally tunable chiral thermal emissions. *Nat. Commun.* **2026**, *17*, 2536. [CrossRef]
36. Kischkat, J.; Peters, S.; Gruska, B.; Semtsiv, M.; Chashnikova, M.; Klinkmüller, M.; Fedosenko, O.; Machulik, S.; Aleksandrova, A.; Monastyrskyi, G.; et al. Mid-infrared optical properties of thin films of aluminum oxide, titanium dioxide, silicon dioxide, aluminum nitride, and silicon nitride. *Appl. Opt.* **2012**, *51*, 6789–6798. [CrossRef]
37. Babar, S.; Weaver, J.H. Optical constants of Cu, Ag, and Au revisited. *Appl. Opt.* **2015**, *54*, 477–481. [CrossRef]
38. Moretti, G.Q.; Cortés, E.; Maier, S.A.; Bragas, A.V.; Grinblat, G. Engineering gallium phosphide nanostructures for efficient nonlinear photonics and enhanced spectroscopies. *Nanophotonics* **2021**, *10*, 4261–4271. [CrossRef]
39. Wang, S.; Kuang, H.; Li, W.; Wang, Y.; Luo, H.; Li, C.; Ge, H.; Wang, Q.; Jia, B. Enhanced Tunability of Dual-Band Chiral Metasurface in the Mid-Infrared Range via Slotted Nanocircuit Design. *Nanomaterials* **2024**, *14*, 979. [CrossRef]
40. Yang, Y.; Zenin, V.A.; Bozhevolnyi, S.I. Anapole-assisted strong field enhancement in individual all-dielectric nanostructures. *ACS Photon.* **2018**, *5*, 1960–1966. [CrossRef]
41. Zeng, X.; Rosenmann, D.; Czaplewski, D.A.; Gao, J.; Yang, X. Mid-infrared chiral metasurface absorbers with split-ellipse structures. *Opt. Commun.* **2022**, *525*, 128854. [CrossRef]
42. Tang, H.; Rosenmann, D.; Czaplewski, D.A.; Yang, X.; Gao, J. Dual-band selective circular dichroism in mid-infrared chiral metasurfaces. *Opt. Express* **2022**, *30*, 20063–20075. [CrossRef]

Disclaimer/Publisher's Note: The statements, opinions and data contained in all publications are solely those of the individual author(s) and contributor(s) and not of MDPI and/or the editor(s). MDPI and/or the editor(s) disclaim responsibility for any injury to people or property resulting from any ideas, methods, instructions or products referred to in the content.